

World Model for Battery Degradation Prediction Under Non-Stationary Aging

Kai Chin Lim¹, Khay Wai See¹

¹Independent Researcher, Australia

kc23.lim@gmail.com, khaywai29@gmail.com

Abstract

Degradation prognosis for lithium-ion cells requires forecasting the state-of-health (SOH) trajectory over future cycles. Existing data-driven approaches can produce trajectory outputs through direct regression, but lack a mechanism to propagate degradation dynamics forward in time. This paper formulates battery degradation prognosis as a world model problem, encoding raw voltage, current, and temperature time-series from each cycle into a latent state and propagating it forward via a learned dynamics transition to produce a future trajectory spanning 80 cycles. To investigate whether physics constraints improve the learned dynamics, a monotonicity penalty derived from irreversible degradation is incorporated into the training loss. Three configurations are evaluated on the Severson LiFePO₄ (LFP) dataset of 138 cells. Iterative rollout halves the trajectory forecast error compared to direct regression from the same encoder. The physics constraint improves prediction at the degradation knee without changing aggregate accuracy.

Keywords: battery state of health, world model, latent dynamics, trajectory forecasting, continual learning, elastic weight consolidation, transformer, PatchTST, LiFePO₄, accelerated charging

1 Introduction

Battery degradation prognosis requires forecasting the state-of-health (SOH) trajectory over future cycles from available cycling measurements. Existing data-driven approaches such as Long Short-Term Memory (LSTM), Gated Recurrent Unit (GRU), and transformer models can map a window of cycle measurements to SOH estimates and can produce trajectory outputs through direct regression from a learned representation. These approaches lack a mechanism to propagate degradation dynamics forward in time, and the resulting trajectory predictions learn an average slope applied uniformly across all horizons.

This paper formulates battery degradation prognosis as a world model problem. The architecture encodes raw voltage, current, and temperature time-series from each cycle into a latent state via a 1-D convolutional encoder and a PatchTST transformer, then propagates the latent state forward through a learned dynamics transition. A shared decoder maps each propagated state to an SOH value, producing both a current estimate and a future trajectory spanning 80 cycles from a single architecture trained end to end. To investigate whether physics constraints improve the learned dynamics, a monotonicity penalty derived from irreversible degradation is incorporated into the training loss.

Three world model configurations are evaluated on the Severson LFP dataset [1] of 138 cells aged under fast charging protocols: rollout with physics constraint, rollout without physics constraint, and the encoder backbone evaluated with direct regression. Two control tests complement the study: a plain LSTM baseline and a continual learning configuration using Elastic Weight Consolidation (EWC) across manufacturing batches.

The ablation identifies iterative latent rollout as the essential component for trajectory prognosis. Rollout halves the forecast error at horizon 5 compared to direct regression from the same encoder, and the error grows with horizon as expected from genuine iterative propagation. Direct regression produces flat error across all horizons, consistent with a learned average slope. The physics constraint improves prediction at the degradation knee without changing aggregate accuracy. Continual learning with EWC across manufacturing batches yields 3.3 times worse accuracy than joint training, confirming that EWC provides no benefit when sequential batches share the same data distribution. Fisher information computed after convergence yields near zero values, making EWC functionally inactive. Computing Fisher at a fixed midtraining epoch resolves this.

Section 2 reviews related work. Sections 3 and 4 describe the architecture and experimental setup. Section 5 presents the results. Section 6 discusses the findings.

2 Related Work

2.1 Data-Driven SOH Estimation

Recurrent neural networks, in particular LSTM and GRU, have been widely applied to battery SOH estimation from cycling data. These models accept a window of cycle measurements and output a scalar SOH estimate. Performance on held out cells from the same dataset is competitive with model-based methods. These architectures assume that training and test data are drawn from the same distribution, an assumption that breaks down in sequential aging scenarios.

Severson et al. [1] demonstrated that early-cycle discharge features contain sufficient information to predict end-of-life for LFP cells, establishing the Severson dataset as a standard benchmark for battery lifetime prediction. Their work addressed a different task from per-cycle SOH tracking, predicting total cycle life from the first 100 cycles. The present work uses the same dataset but targets per-cycle SOH estimation and future trajectory forecasting across the full aging lifetime. Gu et al. [2] proposed a CNN-Transformer for SOH estimation, combining convolutional local feature extraction with transformer global attention. Yunusoglu et al. [3] apply a transformer to battery capacity estimation, achieving competitive accuracy on single step SOH outputs.

Model-based approaches including Kalman filter variants have been applied to battery state estimation [4]. These require accurate system models and manual tuning for each cell chemistry. Data-driven methods learn directly from cycling measurements.

2.2 Physics-Informed Machine Learning for Batteries

Physics-informed neural networks (PINNs) [5] incorporate physical constraints into the training loss as soft penalties, without requiring the network to explicitly solve the governing equations at inference time. Applied to batteries, constraints derived from electrochemical models can regularise learned trajectories toward physically consistent behaviour. Wang et al. [6] demonstrated that embedding electrochemical degradation dynamics directly into the loss function stabilises SOH estimation and prognosis from partial charge/discharge curves. Borah et al. [7] survey the integration of physics-based and machine learning models across state estimation, health monitoring, and safety diagnostics, identifying resistance growth modelling as a key open area.

The Single Particle Model (SPM) [8] reduces the electrochemical dynamics of a lithium-ion cell to a single spherical particle per electrode. Under the SPM, internal resistance grows with cycling according to a power-law relationship with SOH: $R/R_0 \sim (1/\text{SOH})^\gamma$, where R_0 is the initial resistance and γ is a chemistry-specific exponent. For LFP chemistry, $\gamma \approx 0.75$ [9]. This relationship provides a direct constraint between observable resistance and predicted SOH.

2.3 Continual Learning

Catastrophic forgetting [10] describes the tendency of neural networks to overwrite weights learned on one task when trained sequentially on a second task. Elastic Weight Consolidation (EWC) [11] addresses forgetting by adding a quadratic penalty that anchors weights important to prior tasks. Importance is estimated via the diagonal of the Fisher information matrix, approximated as mean squared gradients over the prior task data. EWC has been applied in computer vision and natural language processing. Sayed et al. [12] survey continual learning methods for energy management systems, covering replay, regularisation, and architectural approaches. Application of EWC to sequential battery aging stages has not appeared in the literature.

2.4 World Models

The world model formulation [13, 14] posits an internal model of the environment that predicts future states from current state and action: $s_{t+1} = f(s_t, a_t)$. This framing has been applied primarily in model-based reinforcement learning for planning and imagination. Mao et al. [15] extend world models to physical systems, aligning latent representations with physical quantities and constraining their evolution through known physics equations in robotic control. The formulation does not prescribe a specific encoder or transition architecture; Ha and Schmidhuber [14] use a VAE with an RNN, while Mao et al. [15] use a VQ-VAE with structured dynamics. World models have not been applied to battery degradation prognosis.

3 Methodology

3.1 Problem Formulation

Let a battery cell produce a sequence of per-cycle measurements. At cycle k , the raw observation consists of three time-series recorded during discharge: voltage $V(t)$, current $I(t)$, and temperature $T(t)$, each sampled at ~ 1000 timesteps. Discharge capacity and internal resistance require lab grade equipment and are excluded from the model input.

The model receives a window of $W = 30$ consecutive cycles and produces two outputs:

$$\hat{s}(k) = \text{current SOH at cycle } k \quad (\text{scalar}), \quad (1)$$

$$\hat{s}(k+1 : k+H) = \text{predicted SOH for the next } H = 80 \text{ cycles} \quad (\text{vector} \in \mathbb{R}^H). \quad (2)$$

SOH is defined as the ratio of current discharge capacity to the reference capacity at cycle 2, following the normalisation convention of [1].

3.2 World Model Architecture

The architecture is illustrated in Figure 1. Four components transform the input window into the dual output.

Cycle Encoder. Each cycle’s raw time-series $[V(t), I(t), T(t)] \in \mathbb{R}^{3 \times T_{\max}}$ (where $T_{\max} = 1000$) is processed independently by a shared 1-D convolutional neural network. The encoder consists of three Conv1d layers (channels $32 \rightarrow 64 \rightarrow 128$, kernels $7/5/3$, stride 2) with batch normalisation and ReLU activation, followed by adaptive average pooling and a linear projection to a d -dimensional embedding $\mathbf{e}(k) \in \mathbb{R}^d$, where $d = 64$. This produces a fixed-size representation per cycle regardless of the raw time-series length, capturing discharge curve shape, voltage plateau characteristics, and thermal signatures.

PatchTST Encoder. The sequence of cycle embeddings $[\mathbf{e}(k-W+1), \dots, \mathbf{e}(k)] \in \mathbb{R}^{W \times d}$ is divided into patches of length $P = 6$ cycles with stride $S = 3$, following the PatchTST formulation [16]. Each patch is linearly projected to a d -dimensional token. Sinusoidal positional encodings are added. A multihead self-attention transformer encoder with $L = 3$ layers, $N_h = 4$ heads, and feedforward dimension $d_{\text{ff}} = 256$ processes the token sequence, learning relationships between patches at different temporal positions. The output is pooled via adaptive average pooling to a single vector $\mathbf{z}(k) \in \mathbb{R}^d$, representing the latent degradation state at cycle k .

Dynamics Transition. The action vector $\mathbf{u}(k)$ at the last observed cycle encodes the charging current (I_{mean}), the operating condition that varies across cells in the fast charging dataset. A two-layer MLP with residual connection computes the next latent state:

$$\mathbf{z}(k+1) = \mathbf{z}(k) + \text{MLP}([\mathbf{z}(k) \parallel \mathbf{u}(k)]), \quad (3)$$

where $[\cdot \parallel \cdot]$ denotes concatenation. The residual connection enforces that $\mathbf{z}(k+1)$ departs from $\mathbf{z}(k)$ by a learned increment, reflecting the physical intuition that degradation is a continuous process with bounded per-cycle change. Iterating Equation (3) for H steps produces the rollout sequence $\{\mathbf{z}(k+1), \dots, \mathbf{z}(k+H)\}$.

Output Head. A shared decoder maps latent states to SOH:

$$\hat{s}(k) = \text{head}_{\text{current}}(\mathbf{z}(k)), \quad (4)$$

$$\hat{s}(k+h) = \text{head}_{\text{current}}(\mathbf{z}(k+h)), \quad h = 1, \dots, H. \quad (5)$$

A single shared head (two-layer MLP with ReLU) maps any latent vector to a scalar SOH estimate. The future trajectory is obtained by applying this head to each step of the dynamics rollout.

3.3 Training Objective

The total training loss combines up to three terms:

$$\mathcal{L} = \mathcal{L}_{\text{data}} + \lambda_{\text{phys}} \mathcal{L}_{\text{phys}} + \lambda_{\text{EWC}} \mathcal{L}_{\text{EWC}}, \quad (6)$$

World Model Architecture

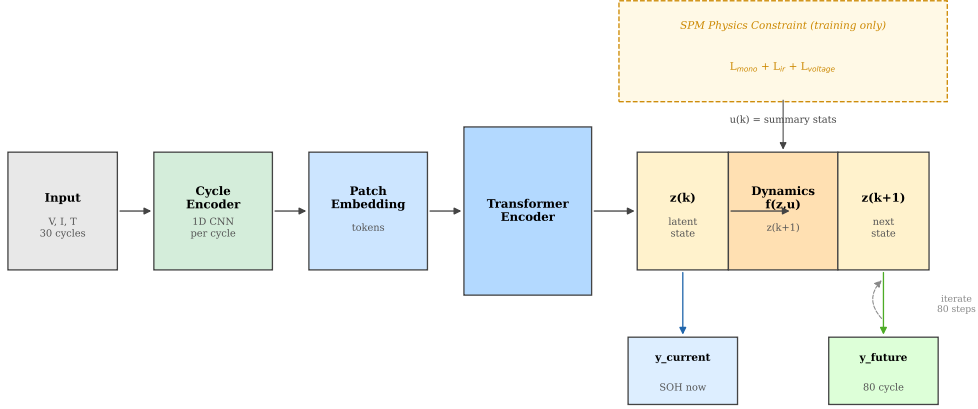


Figure 1. World model architecture. Raw V/I/T time-series per cycle are encoded by a shared 1-D CNN, then processed by PatchTST to produce latent state $\mathbf{z}(k)$. The dynamics module rolls out future latent states and a shared head decodes SOH at each step. The physics constraint operates during training only.

where $\lambda_{\text{phys}} = 0.1$ and $\lambda_{\text{EWC}} = 0.4$. Each term can be independently disabled for ablation as described in Section 5.

Data loss. Mean squared error on current SOH and future trajectory:

$$\mathcal{L}_{\text{data}} = \text{MSE}(\hat{s}(k), s(k)) + \text{MSE}(\hat{\mathbf{s}}(k+1 : k+H), \mathbf{s}(k+1 : k+H)). \quad (7)$$

3.4 Physics Constraint

The physics constraint $\mathcal{L}_{\text{phys}}$ enforces physically consistent trajectory predictions through three terms:

Monotonicity loss $\mathcal{L}_{\text{mono}}$. SOH degradation is irreversible under normal cycling. The predicted future trajectory must be nonincreasing:

$$\mathcal{L}_{\text{mono}} = \frac{1}{H-1} \sum_{h=1}^{H-1} \max(0, \hat{s}(k+h+1) - \hat{s}(k+h) + \varepsilon)^2, \quad (8)$$

where $\varepsilon = 0.005$ is a tolerance for measurement noise.

Resistance to SOH consistency loss \mathcal{L}_{ir} . The SPM predicts that internal resistance grows with cycling as:

$$\frac{R}{R_0} \sim \left(\frac{1}{\text{SOH}} \right)^\gamma, \quad \gamma = 0.75 \text{ (LFP, A123 cell)}, \quad (9)$$

where R_0 is the initial resistance. The SOH implied by the observed resistance ratio is:

$$s_{\text{IR}} = \left(\frac{R_0}{R_{\text{last}}} \right)^{1/\gamma}. \quad (10)$$

The resistance to SOH consistency loss penalises the deviation of the predicted current SOH from the SPM-implied value:

$$\mathcal{L}_{\text{ir}} = \text{MSE}(\hat{s}(k), s_{\text{IR}}). \quad (11)$$

Voltage consistency loss $\mathcal{L}_{\text{voltage}}$. A relative check on terminal voltage consistency with observed current and resistance, serving as a structural regulariser.

The composite physics loss is:

$$\mathcal{L}_{\text{phys}} = \mathcal{L}_{\text{mono}} + \mathcal{L}_{\text{ir}} + \mathcal{L}_{\text{voltage}}. \quad (12)$$

The effect of enabling and disabling $\mathcal{L}_{\text{phys}}$ is reported in Section 5.

3.5 Elastic Weight Consolidation

EWC [11] prevents catastrophic forgetting by penalising changes to weights that were important for prior data. After training on data subset t , the importance of each weight θ_i is estimated by the diagonal Fisher information:

$$F_i \approx \frac{1}{N} \sum_{n=1}^N \left(\frac{\partial \mathcal{L}_{\text{data}}^{(n)}}{\partial \theta_i} \right)^2, \quad (13)$$

where the sum is over N mini-batches. During training on the next subset, the EWC penalty is:

$$\mathcal{L}_{\text{EWC}} = \sum_i F_i (\theta_i - \theta_i^*)^2, \quad (14)$$

where θ_i^* are the weights at the end of the previous subset.

Fisher timing. Fisher must be computed before the model reaches convergence. At convergence, gradients approach zero and $F_i \approx 0$ for all i , making \mathcal{L}_{EWC} functionally inactive. The observed ratio $\mathcal{L}_{\text{EWC}}/\mathcal{L}_{\text{data}} \approx 10^{-4}$ when Fisher is computed postconvergence confirms that the penalty has no effect. Fisher is computed at epoch 10 during each training phase, when gradients remain nontrivial. This is nonstandard relative to the original EWC formulation but is necessary for the mechanism to activate.

Deployment framing. In the primary training configuration described in Section 4, all data is available simultaneously and EWC is not used. EWC is evaluated separately in a batch-staged configuration that simulates deployment where battery populations arrive sequentially and historical data is discarded after each batch.

3.6 Model Variants and Controls

Three configurations form the architecture ablation, isolating the contribution of the dynamics rollout and the physics constraint:

- **PIWM** (Physics-Informed World Model): $\mathcal{L}_{\text{data}} + \lambda_{\text{phys}}\mathcal{L}_{\text{phys}}$. Dynamics rollout active. Physics active. Single pass joint training.
- **WM** (World Model): $\mathcal{L}_{\text{data}}$ only. Dynamics rollout active. Physics disabled. Single pass joint training. Tests whether the physics constraint contributes beyond the data-driven objective.
- **CNN-PatchTST**: $\mathcal{L}_{\text{data}}$ only. Dynamics module removed; future trajectory predicted by direct MLP regression from $\mathbf{z}(k)$ in a single forward pass. Single pass joint training. This is the shared encoder backbone (1-D CNN cycle encoder + PatchTST transformer) evaluated without any world model machinery. It isolates the contribution of latent space rollout.

Two control tests are evaluated separately from the architecture ablation:

- **PIWM + EWC**: $\mathcal{L}_{\text{data}} + \lambda_{\text{phys}}\mathcal{L}_{\text{phys}} + \lambda_{\text{EWC}}\mathcal{L}_{\text{EWC}}$. Same PIWM architecture, trained sequentially across three manufacturing batches (batch 1 \rightarrow batch 2 \rightarrow batch 3) with EWC protecting previous-batch knowledge. Tests whether continual learning improves over joint training when sequential batches share the same data distribution.
- **LSTM**: A two-layer LSTM baseline trained on the same data provides a comparison against standard recurrent approaches. The LSTM produces a single scalar SOH estimate and cannot generate trajectory forecasts.

4 Experimental Setup

4.1 Dataset

Experiments use the Severson et al. LFP dataset [1], comprising 138 LiFePO₄ cells, specifically A123 APR18650M1A with 1.1 Ah nominal capacity, from three manufacturing batches. Cells were cycled to end of life under various fast charging protocols at constant discharge and 30°C chamber temperature. Each cell provides per-cycle raw time-series of voltage, current, and temperature sampled at approximately 1000 timesteps per cycle, as well as lab grade measurements of discharge capacity and internal resistance.

Following [1], cycle 1 is excluded due to known data quality issues. SOH for each cell is normalised by the discharge capacity at cycle 2, which serves as the reference cycle. Two cells from batch 1, cells 0 and 18, are excluded due to equipment failure, leaving 138 usable cells across three batches: 44 from batch 1, 48 from batch 2, and 46 from batch 3.

The 138 cells are split at the cell level into 110 training, 14 validation, and 14 test cells. The split is stratified by minimum SOH reached, ensuring that cells with deep degradation are represented in all partitions. No cycle from a test cell appears in training.

4.2 Input Representation

The model input per cycle consists of raw time-series for voltage, current, and temperature, each padded or truncated to $T_{\max} = 1000$ timesteps. Discharge capacity Q_d and internal resistance IR, which require lab grade coulomb counting and impedance measurement respectively, are excluded from the model input.

The charging current I_{mean} is computed per cycle and used as the action vector $\mathbf{u}(k)$ for the dynamics transition.

Sliding windows of $W = 30$ consecutive input cycles with future target horizon $H = 80$ cycles are constructed within each cell. No cross-cell windows are created. The horizon is selected from a sweep over $H \in \{50, 80, 100\}$: $H=80$ yields the lowest overall MAE (0.006 vs 0.007 for both alternatives) by balancing exposure to the degradation knee (10.9% of windows cross SOH 0.95) against rollout error accumulation at longer horizons.

4.3 Training Protocol

The primary training configuration is single pass: all training data is loaded into a single DataLoader, shuffled every epoch, and processed with standard gradient descent. The Adam optimiser [17] is used with learning rate 10^{-3} and weight decay 10^{-4} . Early stopping terminates training after 15 epochs without validation MAE improvement, with a maximum of 100 epochs. Gradients are clipped to ℓ_2 norm 1.0.

Imbalance handling. The SOH distribution is heavily skewed: 83% of samples fall above SOH 0.95, 11% between 0.90 and 0.95, and 6% between 0.85 and 0.90. Inverse-frequency sampling across four aging stages ensures balanced representation per batch, preventing the model from learning a constant healthy-cell predictor.

Batch-staged EWC configuration. For the continual learning experiment in Section 5, the same architecture is trained sequentially across three manufacturing batches (batch 1 \rightarrow batch 2 \rightarrow batch 3), with EWC applied between batches. Fisher information is computed at epoch 10 of each batch phase. Inverse-frequency sampling is applied within each batch to handle SOH imbalance. This configuration simulates deployment where each battery population arrives over time and historical data from previous batches is discarded.

Hyperparameters are fixed across all variants: $\lambda_{\text{phys}} = 0.1$, $\lambda_{\text{EWC}} = 0.4$, window $W = 30$, horizon $H = 80$, batch size 32, $d = 64$.

4.4 Baselines

The LSTM baseline is a two-layer LSTM with hidden size 64 and a two-layer MLP head, trained on the full training set using single pass training with the same data split. The input dimension matches the world model’s summary features. The LSTM produces

a single scalar SOH estimate per input window and cannot produce multistep future trajectory predictions. This is an architectural constraint, not a performance limitation. LSTM results are reported as a control test in Section 5.

4.5 Evaluation Metrics

MAE, RMSE, and MAPE are computed per aging stage and overall for all variants. Aging stages are defined in Table 1. Stage 4 contains insufficient test samples and is excluded from per-stage reporting. Stage 2 corresponds to the degradation knee, where capacity fade accelerates as resistance growth transitions from linear to nonlinear scaling. The knee region is shaded in Figure 2. Subsequent sections refer to this region as the knee.

Table 1. Aging stage definitions.

Stage	SOH range
Stage 1	1.00–0.95
Stage 2	0.95–0.90
Stage 3	0.90–0.85
Stage 4	below 0.85

Future trajectory accuracy is evaluated at horizons $h \in \{5, 10, 20, 50\}$ cycles ahead for the world model variants.

All evaluation uses the 14 held out test cells. The test set is not accessed during training or hyperparameter selection.

5 Results

5.1 Architecture Ablation

Table 2 reports MAE, RMSE, and MAPE on the 14 test cells, broken down by aging stage, for the three architecture variants.

Table 2. Architecture ablation on the test set. All variants use single pass joint training. Lowest values per column are in bold.

Model	Rollout	Physics	MAE	RMSE	MAPE%	S1 MAE	S2 MAE	S3 MAE
PIWM	Yes	Yes	0.0063	0.0097	0.66	0.0056	0.0080	0.0185
WM	Yes	No	0.0063	0.0090	0.65	0.0054	0.0098	0.0135
CNN-PatchTST	No	No	0.0078	0.0112	0.81	0.0071	0.0103	0.0149

Two findings emerge from the architecture ablation.

Removing the dynamics rollout increases overall MAE from 0.0063 to 0.0078, a 24% degradation, and doubles the forecast error at short horizons as shown in Table 3. The

rollout provides a multitask learning benefit even for current SOH estimation. Training on the trajectory objective forces the encoder to produce a richer latent representation than what current step estimation alone requires.

PIWM and WM achieve identical aggregate MAE of 0.0063. RMSE separates them: WM achieves 0.0090 versus 0.0097 for PIWM, indicating that the physics constraint introduces larger outlier errors. Per-stage results locate the effect. PIWM achieves lower error at Stage 2, the degradation knee, with MAE 0.0080 compared to 0.0098 for WM. WM is better at Stage 3, late degradation, with MAE 0.0135 compared to 0.0185 for PIWM. The physics constraint acts as a regulariser at the knee region, reducing Stage 2 error by enforcing monotonic degradation where capacity fade accelerates.

5.2 Future SOH Trajectory Forecast

Table 3 reports future trajectory MAE at horizons 5, 10, 20, and 50 cycles ahead for the architecture variants.

Table 3. Future SOH trajectory MAE at forecast horizons $h \in \{5, 10, 20, 50\}$ cycles ahead.

Model	h5	h10	h20	h50
PIWM	0.0067	0.0072	0.0081	0.0109
WM	0.0065	0.0068	0.0075	0.0096
CNN-PatchTST	0.0136	0.0135	0.0133	0.0134

The critical comparison is between the rollout models and CNN-PatchTST. PIWM achieves MAE of 0.0067 at horizon 5 versus 0.0136 for CNN-PatchTST, a factor of two improvement. This gap is the core evidence that latent space dynamics rollout produces meaningfully better forecasts at short horizons than direct regression from a static latent vector.

CNN-PatchTST shows flat forecast error across all horizons, ranging from 0.0133 to 0.0136. This is consistent with a model that has no mechanism to propagate degradation forward and instead learns a single average trajectory slope applied uniformly. The rollout models show error growing with horizon, from 0.0067 at horizon 5 to 0.0109 at horizon 50, consistent with uncertainty compounding over the rollout window. This growing error profile is a signature of genuine iterative forecasting.

WM achieves slightly better future horizon MAE than PIWM at all horizons, with horizon 50 MAE of 0.0096 versus 0.0109. This is consistent with the physics constraint improving current SOH estimation at the knee region without benefiting trajectory forecasting.

5.3 Trajectory Visualisation

Figure 2 presents per-cell trajectory performance in two complementary views. The top row shows three representative cells selected to illustrate distinct model behaviours. Cell 127 shows the largest rollout advantage, with PIWM achieving MAE 0.002 compared to 0.008 for CNN-PatchTST. Cell 57 exposes the PIWM+EWC failure mode, where batch-staged training produces MAE 0.101 compared to 0.006 for PIWM with joint training. Cell 45 is the shortest lifecycle cell at 169 cycles, where the input window of 30 cycles and verification horizon of 80 cycles leave only 59 evaluable points. Cell 45 reaches SOH 0.90 at cycle 100, faster than any cell in the training set where the earliest SOH 0.90 crossing occurs at cycle 214. The model extrapolates beyond its training distribution on this cell. Forecast wicks, 20 per cell and evenly spaced, show predictions from PIWM 80 cycles ahead, anchored to the prediction line at each origin cycle.

The heatmap in Figure 2 reports MAE for all five methods across all 14 test cells, sorted by degradation depth with the most degraded cells on the left. This exposes failure modes at the cell level that are invisible in aggregate metrics. PIWM achieves MAE below 0.005 on 10 of 14 cells. The highest errors occur on cell 45, the only test cell that degrades outside the training distribution, and on cells where PIWM+EWC fails catastrophically due to batch-staged training.

Every cell loses 110 cycles from evaluation. The first 30 cycles are consumed as the input window, and the last 80 cycles lack sufficient ground truth to verify the full forecast horizon.

5.4 Control Tests

5.4.1 Continual Learning

Table 4 details the batch-staged EWC training progression, showing how performance evolves as each manufacturing batch is incorporated. The same PIWM architecture is used and only the training strategy differs.

Table 4. PIWM + EWC batch-staged training progression. Validation MAE at the end of each batch phase.

Phase	Validation MAE	Early stop epoch
Batch 1	0.023	18
Batch 2	0.057	18
Batch 3	0.014	20
Test	0.021	—

The final test MAE of 0.021 is 3.3 times worse than PIWM with joint training at 0.006. The three manufacturing batches in the Severson dataset share the same cell chemistry,

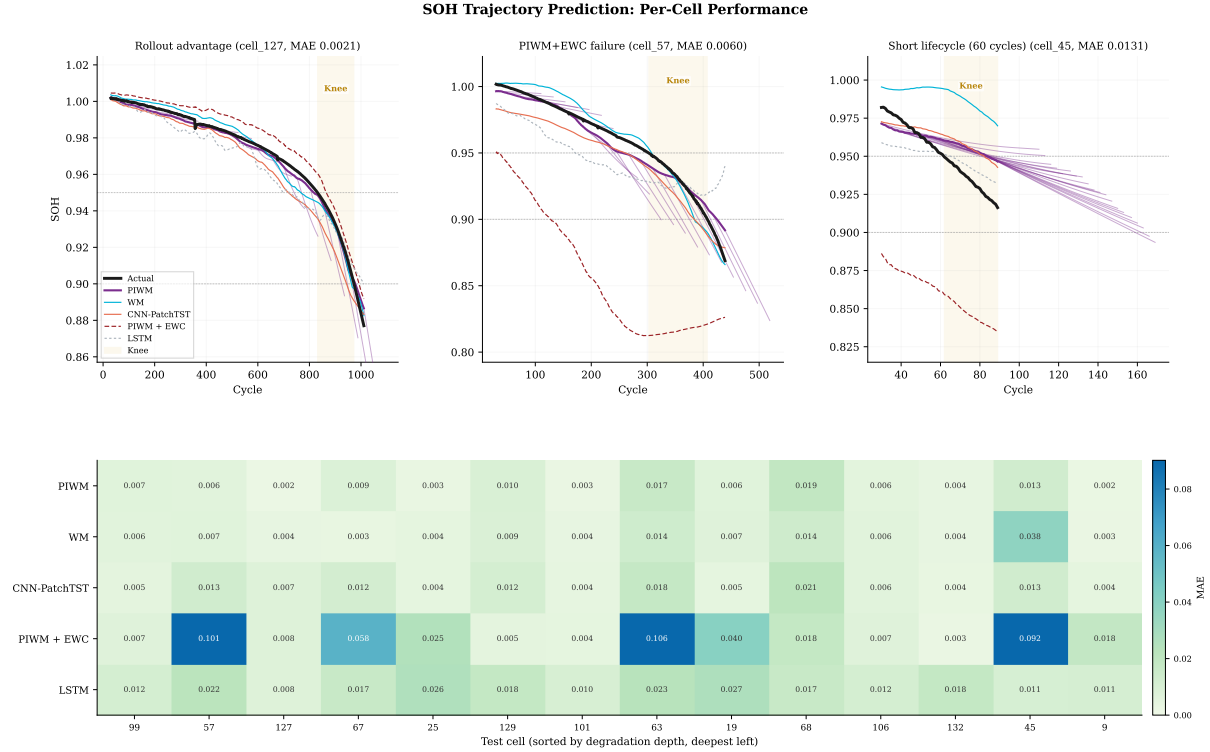


Figure 2. Per-cell SOH trajectory performance. Top row: three representative cells showing rollout advantage on cell 127, PIWM+EWC failure mode on cell 57, and short lifecycle limitation on cell 45. Forecast wicks in purple show 80 cycles ahead predictions from PIWM, 20 wicks per cell. Bottom: MAE heatmap for all five methods across all 14 test cells, sorted by degradation depth.

format, and degradation task. When sequential batches share the same data distribution, the catastrophic forgetting problem that EWC addresses does not arise. Joint training on the combined dataset is strictly superior.

The forgetting analysis shows partial protection. Batch 1 test MAE degrades from 0.004 immediately after batch 1 training to 0.005 after batch 2 and 0.013 after batch 3. EWC slows but does not prevent knowledge erosion across batches.

5.4.2 LSTM Baseline

The LSTM baseline achieves overall MAE 0.0209, 3.3 times worse than PIWM at 0.0063. Table 5 summarises both control tests alongside PIWM for reference.

Table 5. Control tests compared with PIWM under joint training.

Model	Training	MAE	RMSE	MAPE%	S1 MAE	S2 MAE	S3 MAE
PIWM	Joint	0.0063	0.0097	0.66	0.0056	0.0080	0.0185
PIWM + EWC	Batch-staged	0.0210	0.0377	2.19	0.0167	0.0413	0.0341
LSTM	Joint	0.0209	0.0286	2.20	0.0164	0.0344	0.0598

5.5 Latent Space Analysis

Figure 3 shows PCA projections of the latent vectors $\mathbf{z}(k)$ for the four variants that share the CNN-PatchTST encoder, coloured by SOH value. CNN-PatchTST shows multiple separated strands corresponding to individual cells, indicating the encoder retains cell identity rather than learning a shared degradation representation. Both rollout models, PIWM and WM, compress all cells onto a single tight curve ordered by SOH. The transition function requires a unified trajectory to step along, and the rollout training objective forces the encoder to produce this structure. PIWM and WM show similar latent geometry, indicating that the physics constraint does not reshape the latent space. PIWM + EWC shows an inverted arch with more variance in PC2 (4.1% versus 0.7–1.9% for the other variants), indicating that batch-staged training disrupts the latent organisation that joint training produces.

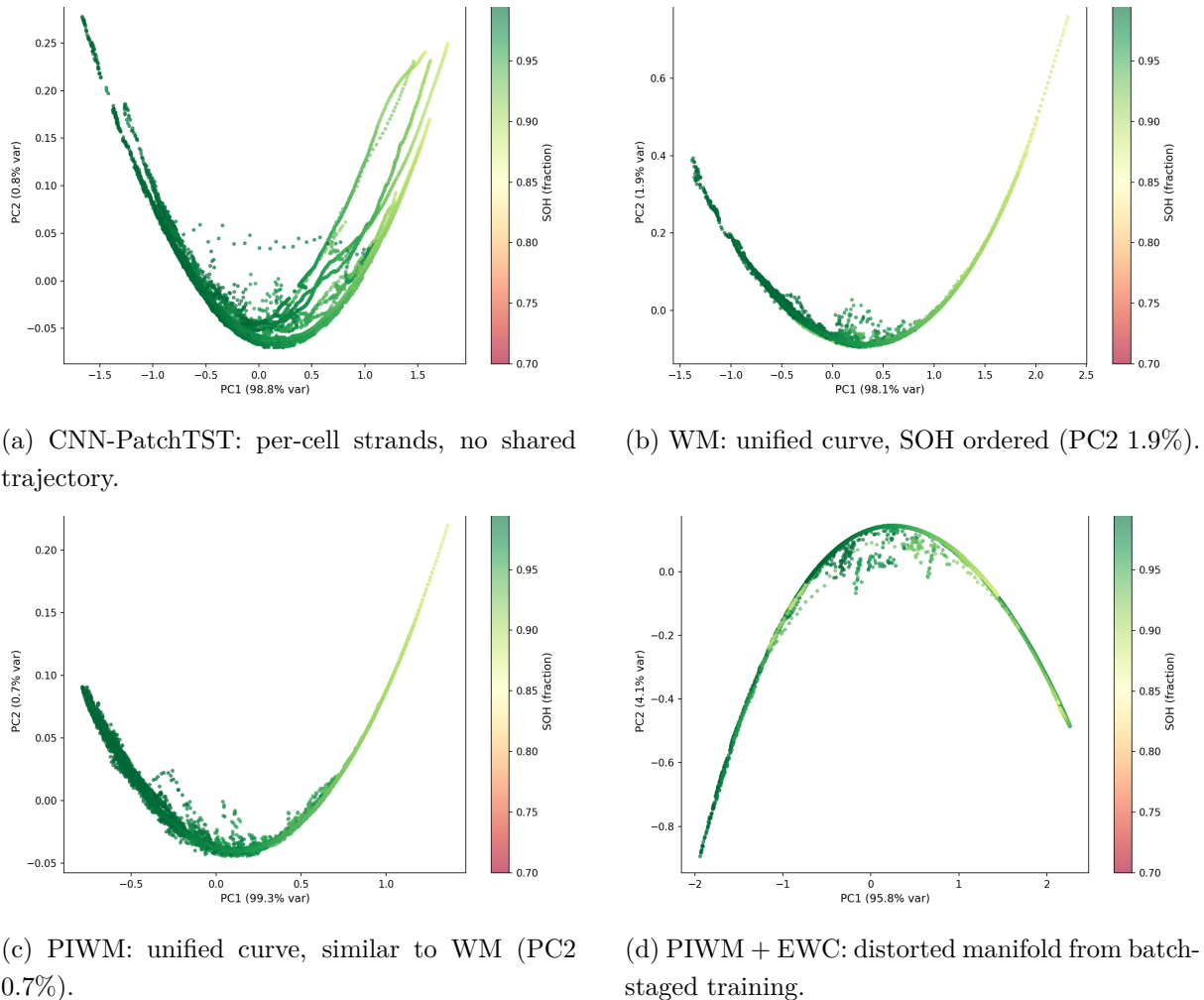


Figure 3. PCA of latent vectors $\mathbf{z}(k)$, coloured by SOH value. The rollout objective produces a unified SOH-ordered curve (b, c), while the encoder without rollout retains per-cell structure (a) and batch-staged training distorts the manifold (d).

6 Discussion

6.1 Effect of the Dynamics Rollout

The rollout improves both current estimation and future forecasting through a multitask learning effect. The rollout objective forces the encoder to produce latent states that encode not only current SOH but also how SOH will evolve. The shared decoder then benefits from this enriched representation even for the current step estimate.

The latent space PCA in Figure 3 provides direct evidence. CNN-PatchTST, trained without rollout, produces per-cell strands in latent space where the encoder retains cell identity. The rollout models compress all cells onto a single SOH-ordered curve. The transition function requires a unified trajectory to step along, and the training objective enforces this structure. This explains why CNN-PatchTST produces flat forecast error across horizons: without a shared trajectory in latent space, the decoder learns a single average slope rather than iterative propagation.

6.2 Physics Constraint as Targeted Regularisation

The monotonicity penalty is most effective at the knee where capacity fade accelerates and the model is prone to predicting temporary SOH recovery. Enforcing nonincreasing trajectories reduces Stage 2 MAE. Below SOH 0.90, the constraint overregularises at Stage 3, increasing both MAE and RMSE.

The RMSE difference between PIWM and WM (0.0097 versus 0.0090) indicates that the physics penalty introduces larger outlier errors. These outliers concentrate at Stage 3 where the constraint is least valid. WM also achieves better future trajectory MAE at all horizons, consistent with the physics penalty adding a small bias that compounds over the rollout window.

The physics constraint weight $\lambda_{\text{phys}} = 0.1$ is untuned. Stage-dependent activation or adaptive balancing such as GradNorm [18] may improve the tradeoff between Stage 2 and Stage 3. This is deferred to subsequent work.

6.3 Continual Learning and Data Distribution

The three manufacturing batches in the Severson dataset share the same cell chemistry, format, and degradation task. When sequential batches are drawn from the same distribution, the catastrophic forgetting problem that EWC addresses does not arise. Joint training is strictly superior because the batches contain redundant, not conflicting, information.

Continual learning would be better motivated when sequential data represents genuinely different distributions, such as different cell chemistries or different operating conditions.

In such settings, new data can destructively interfere with previously learned representations, and EWC parameter protection becomes necessary.

The PCA in Figure 3(d) shows that batch-staged training distorts the latent manifold, with PC2 capturing 4.1% of variance compared to 0.7–1.9% under joint training. The sequential optimisation path produces a qualitatively different latent geometry that the transition function cannot compensate for.

6.4 Generalisation Boundary

Cell 45 degrades faster than any cell in the training set, reaching SOH 0.90 at cycle 100 versus cycle 214 for the fastest training cell. All methods produce higher error on this cell because they extrapolate beyond the training distribution. This is not a model failure but a data coverage boundary: the model cannot be expected to generalise to degradation rates it has never observed.

The test set contains 14 cells with lifecycles ranging from 169 to 1835 cycles. The stratified split by degradation depth ensures coverage across degradation stages, but does not guarantee coverage of all degradation rates. Cell 45 exposes this gap.

6.5 Limitations

The contribution of raw time-series input via the cycle encoder versus summary statistics is not isolated in the current ablation.

The test set contains 14 cells. Stage 3 results are computed over fewer samples and should be interpreted with caution.

All experiments use the Severson LFP dataset. Generalisability to other cell chemistries such as NMC and LCO and to other cycling protocols is not tested. The A123 LFP cell exhibits a relatively flat voltage plateau, which may make the discharge curve shape less informative than for chemistries with more pronounced voltage features such as NMC and NCA.

7 Conclusion

This paper formulated battery degradation prognosis as a world model problem and studied the contribution of iterative latent rollout, a physics constraint, and continual learning on the Severson LFP dataset of 138 cells. The dynamics rollout is the essential component: it halves the forecast error at short horizons and forces the encoder to learn a unified latent trajectory that benefits both SOH estimation and trajectory forecasting. The physics constraint improves prediction at the degradation knee at the cost of late degradation accuracy. EWC continual learning provides no benefit when sequential batches share the

same data distribution. Future work includes adaptive physics constraint balancing, extension to additional cell chemistries, and continual learning across heterogeneous battery populations.

References

- [1] K. A. Severson, P. M. Attia, N. Jin, N. Perkins, B. Jiang, Z. Yang, M. H. Chen, M. Aykol, P. K. Herring, D. Fraggedakis, M. Z. Bazant, S. J. Harris, W. C. Chueh, and R. D. Braatz. Data-driven prediction of battery cycle life before capacity degradation. *Nature Energy*, 4:383–391, 2019. doi: 10.1038/s41560-019-0356-8.
- [2] Xinyu Gu, K. W. See, Penghua Li, Kangheng Shan, Yunpeng Wang, Liang Zhao, Kai Chin Lim, and Neng Zhang. A novel state-of-health estimation for the lithium-ion battery using a convolutional neural network and transformer model. *Energy*, 262:125501, 2022. doi: 10.1016/j.energy.2022.125501.
- [3] Aybars Yunusoglu, Dexter Le, Karn Tiwari, Murat Isik, and I. Can Dikmen. Battery state of health estimation using LLM framework, 2025. arXiv:2501.18123.
- [4] K. Lim, H. A. Bastawrous, V. H. Duong, K. W. See, P. Zhang, and S. X. Dou. Fading Kalman filter-based real-time state of charge estimation in LiFePO₄ battery-powered electric vehicles. *Applied Energy*, 169:40–48, 2016. doi: 10.1016/j.apenergy.2016.01.100.
- [5] M. Raissi, P. Perdikaris, and G. E. Karniadakis. Physics-informed neural networks: A deep learning framework for solving forward and inverse problems involving nonlinear partial differential equations. *Journal of Computational Physics*, 378:686–707, 2019. doi: 10.1016/j.jcp.2018.10.045.
- [6] Fujin Wang, Zhi Zhai, Zhibin Zhao, Yi Di, and Xuefeng Chen. Physics-informed neural network for lithium-ion battery degradation stable modeling and prognosis. *Nature Communications*, 15:4332, 2024. doi: 10.1038/s41467-024-48779-z.
- [7] Manashita Borah, Qiao Wang, Scott Moura, Dirk Uwe Sauer, and Weihan Li. Synergizing physics and machine learning for advanced battery management. *Communications Engineering*, 3:134, 2024. doi: 10.1038/s44172-024-00273-6.
- [8] M. Doyle, T. F. Fuller, and J. Newman. Modeling of galvanostatic charge and discharge of the lithium/polymer/insertion cell. *Journal of the Electrochemical Society*, 140(6):1526–1533, 1993. doi: 10.1149/1.2221597.
- [9] E. Prada, D. Di Domenico, Y. Creff, J. Bernard, V. Sauvant-Moynot, and F. Huet. Simplified electrochemical and thermal model of LFP-graphite Li-ion batteries for fast charge applications. *Journal of the Electrochemical Society*, 159(9):A1508–A1519, 2012. doi: 10.1149/2.064209jes.

- [10] M. McCloskey and N. J. Cohen. Catastrophic interference in connectionist networks: The sequential learning problem. *Psychology of Learning and Motivation*, 24:109–165, 1989.
- [11] J. Kirkpatrick, R. Pascanu, N. Rabinowitz, J. Veness, G. Desjardins, A. A. Rusu, K. Milan, J. Quan, T. Ramalho, A. Grabska-Barwinska, D. Hassabis, C. Clopath, D. Kumaran, and R. Hadsell. Overcoming catastrophic forgetting in neural networks. *Proceedings of the National Academy of Sciences*, 114(13):3521–3526, 2017. doi: 10.1073/pnas.1611835114.
- [12] Aya Nabil Sayed, Yassine Himeur, Iraklis Varlamis, and Faycal Bensaali. Continual learning for energy management systems: A review of methods and applications, and a case study. *Applied Energy*, 384, 2025. doi: 10.1016/j.apenergy.2025.001886.
- [13] R. S. Sutton. Dyna, an integrated architecture for learning, planning, and reacting. *ACM SIGART Bulletin*, 2(4):160–163, 1991. doi: 10.1145/122344.122377.
- [14] D. Ha and J. Schmidhuber. World models. In *Advances in Neural Information Processing Systems*, 2018.
- [15] Zhenjiang Mao, Mrinall Eashaan Umasudhan, and Ivan Ruchkin. Physically interpretable world models via weakly supervised representation learning, 2024. arXiv:2412.12870.
- [16] Y. Nie, N. H. Nguyen, P. Sinthong, and J. Kalagnanam. A time series is worth 64 words: Long-term forecasting with transformers. In *International Conference on Learning Representations*, 2023.
- [17] D. P. Kingma and J. Ba. Adam: A method for stochastic optimization. In *International Conference on Learning Representations*, 2015.
- [18] Z. Chen, V. Badrinarayanan, C. Lee, and A. Rabinovich. GradNorm: Gradient normalization for adaptive loss balancing in deep multitask networks. In *International Conference on Machine Learning*, pages 794–803, 2018.